

Multi-wave parametric X-ray production by relativistic particles in crystals: comparison of computations and experimental results

S.A. Stepanov*, A.Ya. Silenko, A.P. Ulyanenko, I.Ya. Dubovskaya

Institute for Nuclear Problems, 11 Bobruiskaya St., 220050 Minsk, Belarus

Received 19 May 1995; revised form received 8 March 1996

Abstract

The angular distributions of parametric X-ray radiation (PXR) produced by relativistic particles in crystals under the conditions of 4- and 8-wave Bragg diffraction are computed with the help of the method developed recently by Dubovskaya et al. [J. Phys.: Condens. Matter 5 (1993) 7771]. The computations are qualitatively compared to the experimental data known to date. It is shown that the enhancement of PXR intensity observed in the 8-wave experiment [Sov. Phys. – JETP Lett. (USA) 51 (1990) 242] could indeed be due to the multi-wave Bragg effect. The fine structure of multi-wave PXR peaks is analyzed.

1. Introduction

Charged relativistic particles moving with a constant velocity through a solid generate a white spectrum of electromagnetic radiation in a narrow cone $\theta \lesssim m/E$ along the direction of their movement (m and E are the mass and the energy of particles, respectively). If the target possesses a crystalline structure, the Bragg diffraction condition

$$(\mathbf{k} + \mathbf{h})^2 \simeq k^2 \quad (1)$$

can be fulfilled for some wavelength of generated photons and the radiation of particles can be observed at a large angle $2\Theta_B \gg m/E$ to the direction of their motion (\mathbf{k} is the wave vector of emitted photons, \mathbf{h} is the crystal reciprocal lattice vector corresponding to the Bragg planes, and Θ_B is the Bragg angle).

As shown by different authors [1–7], the mechanism of this generation becomes qualitatively different when particles move through a thick perfect crystal where the Bragg diffraction of emitted quanta is *dynamical*. Then, the condition of Cherenkov resonance between the particles and the quanta can be fulfilled ($\hbar = c = 1$):

$$1 - vn_j(\mathbf{k}, \omega) \cos \theta = 0. \quad (2)$$

Here v is the velocity of particles and $n_j(\mathbf{k}, \omega)$ are the refractive indices of X-rays in crystal under the Bragg diffraction. It is well-known that the refractive index of X-rays in amorphous media has an universal form $n(\omega) = 1 - \omega_L^2/2\omega^2$, and it is smaller than unity for all frequencies in the X-ray range (ω_L is the Larmor frequency of media). That means, normally condition (2) cannot be fulfilled for X-rays. However, under the *dynamical* Bragg diffraction the energy spectrum of photons contains a set of energy branches and, consequently, the crystal is characterized by several different refractive indices $n_j(\mathbf{k}, \omega)$ (for each energy branch j). Some of these refractive indices can become greater than unity and, consequently, condition (2) can be fulfilled. In other words, the phase velocity of X-rays in crystal normally being greater than the light speed constant can

* Corresponding author. Tel. +49 30 20366 220, fax +49 30 204 4536, e-mail stepanov@x-ray0.roen.ipp-garching.mpg.de.

decrease due to the dynamical Bragg diffraction and the emitted X-rays can move in the Cherenkov resonance with radiating relativistic particles (the particles are assumed to be fast enough: $E \gtrsim 100$ MeV).

The Cherenkov resonance results in the large enhancement of the spectral-angular density of radiation: the number of X-ray quanta generated per electron in this effect varies in the range 10^{-3} – 10^{-6} depending on the diffraction geometry and the particle energy, and the radiation is concentrated within narrow spectral and angular intervals of the order of $(\Delta\omega/\omega, \Delta\theta) \sim |\chi_0|^{1/2} \sim 10^{-2}$ – 10^{-4} (χ_0 is the zero Fourier component of the dielectric susceptibility of crystal). Due to these unique peculiarities, this quasi-Cherenkov radiation became the subject of many theoretical [1–13] and experimental [14–19] studies where it was called the parametric X-ray radiation (PXR).

The Cherenkov resonance can be weak for thin or non-perfect crystals where the dynamical diffraction process is negligible [20] or for particles with relatively low energies when the Cherenkov condition can be fulfilled only very far from the Bragg peak [21–23]. Then the major contribution to the PXR comes from the Bragg effect and the application of the kinematic diffraction theory gives acceptable results being in a good agreement with experimental data [21–23], although the dynamical diffraction approach is applicable as well since it is more general. To distinguish the two different mechanisms of PXR, the radiation at low energies of a few MeV is sometimes called PXR of type B [24]. However, the term PXR is also used, what can lead to a confusion.

The high spectral-angular density and other peculiarities of PXR can provide the applications of this effect as a source of quasi-monochromatic X-rays with tunable wavelength. Lately, the interest in these applications has increased [23–26]. So, the detailed investigation of the characteristics of PXR is very urgent.

The previous theoretical investigations [12,13] have shown the possibility to enhance the PXR spectral-angular density under the conditions of multiple Bragg diffraction [27], where the emitted X-rays make the Bragg angles with several atomic planes in crystal simultaneously (condition (1) is fulfilled for several different h). The 4- and 8-wave experiments carried out in Refs. [17,19] also revealed some anomalies in PXR angular distributions that were attributed to the multiple Bragg diffraction effect. In particular, an intense narrow peak was observed in the 8-wave experiment.

Evidently, these facts are very important for the applications of PXR as a monochromatic X-ray source. Therefore, we made a serious attempt to develop the method of computing PXR spectral-angular spectra under multi-wave diffraction [13]. Our algorithm reported in Ref. [13] is based on the numerical methods used in the dynamical theory of X-ray multiple Bragg diffraction [28,29]. In Ref. [13], the validity of this algorithm was illustrated with the computations of PXR angular spectra for forbidden Bragg reflection (222) simulated by 3-wave diffraction in a germanium crystal. It was shown that the proposed method was capable of treating an arbitrary multi-wave case of PXR.

The present article is devoted to the computation of 4- and 8-wave PXR angular spectra with the help of the model reported in Ref. [13]. The computed angular spectra are compared to the respective two-wave angular spectra in order to demonstrate the multi-wave diffraction contributions, and to the experimental data reported in Refs. [17,19] (Sections 4 and 5, respectively). As not all the parameters of the experiments are available, we carry out a qualitative comparison in order to prove that the multiple Bragg diffraction effects could really be the origin of the observed anomalies. The application of the dynamical diffraction theory is argued by the two factors. First, the conditions of experiments [17,19] presume the dynamical Bragg diffraction and the dominating role of the quasi-Cherenkov effect. Second, the analysis of interaction between different Bragg peaks at multiple Bragg diffraction can only be done in the frame of the dynamical diffraction theory: by definition, the kinematical theory does not take into account the effects of the Bragg peaks on each other.

To initiate the discussion, a short outline on 4- and 8-wave experiments [17,19] and a summary of the theory [13] are given in Sections 2 and 3, respectively.

2. Experimental data on 4- and 8-wave PXR production

The measurements of the angular distributions of parametric X-ray radiation were carried out at synchrotron “Sirius” in Tomsk for the electron beam with energies 500 MeV (4-wave experiment) and 900 MeV (8-wave

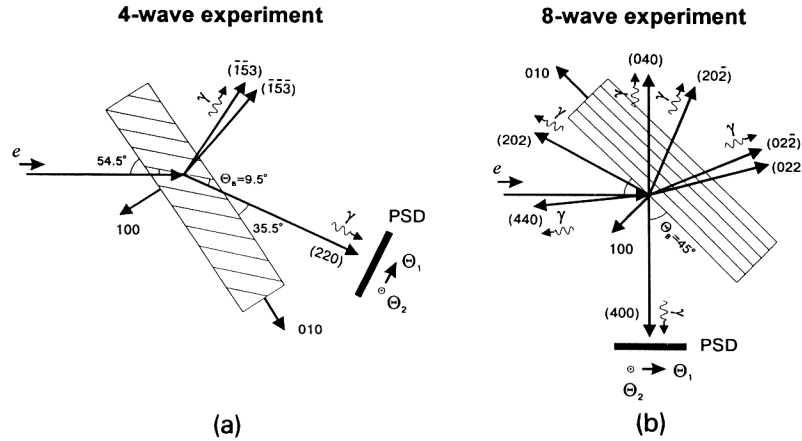


Fig. 1. Schematic layouts of 4-wave (a) and 8-wave (b) PXR experiments. e is the incident relativistic electron beam, γ are parametric X-rays exiting the crystal along the Bragg directions. PSD is the position sensitive detector registering one of the Bragg reflected X-ray beams. The angles Θ_1 and Θ_2 are varied along PSD rule and perpendicularly to the picture plane. Θ_B indicates the Bragg angle for the measured reflection.

experiment). The schematic layout of the experiments is shown in Fig. 1. A GaAs single crystal plate 400 μm thick cut parallel to the (100) plane was set up on the goniometer in such a way that the electron beam moved through it nearly along the incidence direction for 4-beam Bragg diffraction (000), (220), ($\bar{1}\bar{5}\bar{3}$), ($\bar{1}\bar{5}\bar{3}$) of X-rays with $\lambda = 0.6708 \text{ \AA}$ in experiment [17], and for 8-beam diffraction (000), (400), (022), ($0\bar{2}\bar{2}$), ($20\bar{2}$), ($0\bar{4}0$), (440) of X-rays with $\lambda = 1.9987 \text{ \AA}$ in Ref. [19] (in the latter case the incidence direction coincided with $\langle 110 \rangle$ crystallographic axis). In these cases, three X-ray beams were expected to exit the crystal at large angles to the electron beam in Ref. [17] and seven ones in Ref. [19]. The experiments were aimed to reveal the changes in one of these Bragg reflected PXR beams due to the other beams. Therefore, only one PXR beam corresponding to the Bragg planes (220) and (400) was registered in Refs. [17,19], respectively. The radiation was detected by a linear position sensitive detector (PSD). A series of PXR angular distributions as functions of the angle Θ_1 on the PSD rule were measured while varying the angle Θ_2 by linear displacements of the detector (see Fig. 1).

The main parameters describing the experimental conditions are presented in Table 1 and the PXR angular distributions measured in the experiments [17,19] are shown in Figs. 2 and 3a, respectively.

The PXR angular distribution in Fig. 2 corresponding to 4-wave Bragg diffraction geometry displays an asymmetry in the height of the right and left peaks. That is contrary to the case of two-wave PXR generation where the peaks are symmetrical [6].

In the case of 8-wave PXR generation (Fig. 3a), one can see prominent asymmetry of two peaks (the left peak is 2.5 times higher than the right one) and the splitting of the left peak into two parts. For comparison,

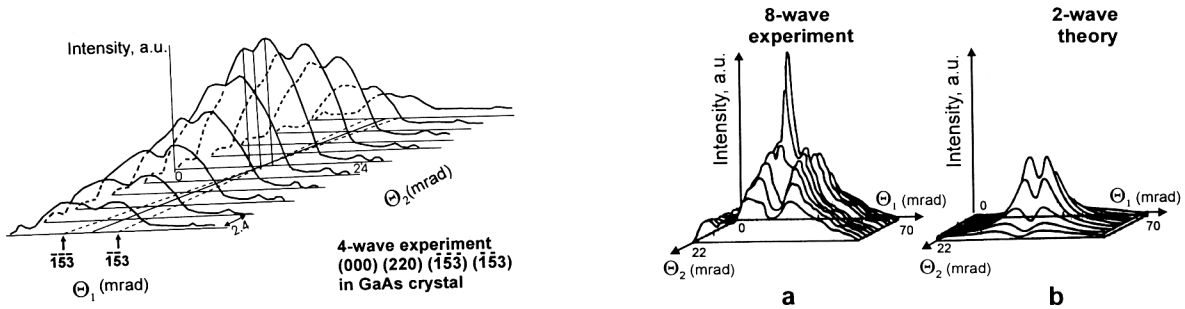


Fig. 2. (Left) The PXR angular distribution for (220) reflection in GaAs measured in Ref. [17] under 4-wave diffraction conditions.

Fig. 3. (Right) The PXR angular distribution for (400) reflection in GaAs. (a): the experimental distribution measured in Ref. [19] under 8-wave diffraction conditions, (b): the theoretical distribution calculated in 2-wave approximation.

Table 1

Some experimental parameters from Refs. [17,19]. Here E and λ are the energy and the wavelength of generated X-ray quanta, $\Delta\theta_1$ and $\Delta\theta_2$ are the angular resolutions in the directions along the detector rule and normal to it; Θ_s is the mean square angle of electron's multiple scattering inside the crystal

Experiment	Bragg planes	E [keV]	λ [Å]	$\Delta\theta_1$ [mrad]	$\Delta\theta_2$ [mrad]	Θ_s [mrad]
4-wave	(000), (220), ($\bar{1}\bar{5}\bar{3}$), ($\bar{1}\bar{5}3$)	18.4	0.670765	0.1	1.0	2.5
8-wave	(000), (400), (022), (02 $\bar{2}$), (202), (20 $\bar{2}$), (040), (440)	6.2	1.9987	0.3	3.0	7.0

the respective two-wave angular distribution calculated under the same experimental conditions is presented in Fig. 3b.

These specific features were supposed by the authors of the experiments to be the manifestation of multi-wave generation of PXR, although the simulation of these experiments was not carried out.

Below we give the results of our numerical simulations of these experiments and try to compare the experimental and theoretical data.

3. Theory

The basics of PXR dynamical theory were first derived in Ref. [1] (a correction was given in Ref. [2]) and then were multiply repeated on the basis of both quantum and classical considerations (see, e.g. Refs. [4–6,3,11,30–33]). Both approaches as well as alternative works [7–10] brought essentially the same results.

Though all the mentioned works were confined with the 2-beam PXR, the basic equations are general and valid for multi-beam PXR too. The X-ray field produced by a moving relativistic particle can be calculated as a convolution of the Green function of the problem with a current density produced by the particle. The calculations are greatly simplified by the expansion of the Green function into a series of solutions to *inverse homogeneous* X-ray diffraction problem in crystal. The substitution of this expansion into the convolution integral allows us to obtain the following expression for a number of PXR quanta emitted by a particle, for example, in a Bragg reflection \mathbf{h} (we assume $\hbar = c = 1$):

$$dN_{n,\omega}^s = \left(\frac{e\omega}{2\pi} \right)^2 \left| \int_{t_0}^{t_1} \mathbf{E}_{-\mathbf{k}}^{(+s)}(\mathbf{r}(t), \omega) \cdot \mathbf{v}(t) e^{i\omega t} dt \right|^2 \frac{d\omega}{\omega} d\Omega. \quad (3)$$

Here $\mathbf{r} = \mathbf{v}t$ is the coordinate vector and \mathbf{v} is the velocity vector of the particle; $\omega = |\mathbf{k}|$, and $\mathbf{k} = -(\omega\mathbf{v} + \mathbf{h})$ is the wave vector of an “inverted” X-ray photon, i.e. the photon incident onto the crystal from the point of observation of parametric X-rays emitted by the particle in the Bragg reflection \mathbf{h} . Finally, $\mathbf{E}_{-\mathbf{k}}^{(+s)}$ is the wavefield produced by this photon in crystal, index s denotes σ - and π -polarizations, and $d\omega$ and $d\Omega$ are the spectral and angular intervals where the X-rays are detected. The integration in Eq. (3) is carried out over the whole interval of particle motion through the crystal.

Eq. (3) was the starting one in our previous work [13], as well as in some other works [31,33]. We derive this equation in Appendix A since the lack of this derivation sometimes caused doubts in its correctness.

As shown in Ref. [13], the wavefields $\mathbf{E}_{-\mathbf{k}}^{(+s)}$ can be found with the help of numerical methods developed in the dynamical theory of multiple Bragg diffraction [28,29]. Under the multiple Bragg diffraction, the X-ray wave field $\mathbf{E}_{-\mathbf{k}}^{(+s)}(\mathbf{r}, \omega)$ inside a crystal can be represented as a sum of transverse Bloch waves which travel in all the Bragg diffraction directions $\mathbf{k}_m = \mathbf{k}_m + \mathbf{m}$ and correspond to $2N$ -dispersion branches [28,29] (N is the order of multiple Bragg diffraction):

$$\mathbf{E}_{-\mathbf{k}}^{(+s)}(\mathbf{r}, \omega) = \mathbf{e}_m^s \sum_m \mathcal{D}_m^s(\mathbf{r}), \quad (4)$$

$$\mathcal{D}_m^s(\mathbf{r}) = \sum_{j=1}^{2N} \lambda^{(j)} D_m^{s(j)} \exp(i [\mathbf{k}_m - \omega(\epsilon^{(j)} - \alpha_m) \mathbf{n}] \mathbf{r}). \quad (5)$$

Here the parameters $\alpha_m = [(\mathbf{k}_0 + \mathbf{m})^2 - \omega^2]/2\omega^2\gamma_m$ determine the deviation of incident wave from the exact Bragg condition for the respective reflection; γ_m are the cosines of the angles between the X-ray wave vectors and the internal normal to the crystal surface. The parameters $\lambda^{(j)}$ are the coefficients of excitation of different dispersion branches, $D_m^{s(j)}$ are the field amplitudes for each branch, and $\epsilon^{(j)}$ determine the refraction of X-ray Bloch waves of different branches as a function of α_m .

The wave amplitudes $D_m^{s(j)}$ and the parameters $\epsilon^{(j)}$ can be found as eigen vectors and eigen values of the dynamical diffraction equations which have the form [28,29]:

$$\sum_{s'=\sigma,\pi} \sum_{m'=1,N} G_{mm'}^{ss'} D_{m'}^{s'(j)} = \epsilon^{(j)} D_m^{s(j)}, \quad (6)$$

where:

$$G_{mm'}^{ss'} = \alpha_m \delta_{mm'}^{ss'} - \left(\frac{1}{2\gamma_m} \right) \left\{ \chi_{mm'} (\mathbf{e}_m^s \cdot \mathbf{e}_{m'}^{s'}) + i\chi_{mm'}^Q [(\mathbf{k}_m \cdot \mathbf{k}_{m'}) (\mathbf{e}_m^s \cdot \mathbf{e}_{m'}^{s'}) + (\mathbf{e}_m^s \cdot \mathbf{k}_{m'}) (\mathbf{k}_m \cdot \mathbf{e}_{m'}^{s'})] / \omega^2 \right\} \quad (7)$$

is the $2N \times 2N$ scattering matrix, $\chi_{mm'}$ and $\chi_{mm'}^Q$ are the dipole and quadrupole components of the expansion of crystal dielectric susceptibility $\chi(\mathbf{r}, \omega)$ in a Fourier series over the reciprocal lattice vectors.

Finally, the coefficients $\lambda^{(j)}$ are given by the boundary conditions. For a plate-shaped crystal these conditions are reduced to the system of linear equations:

$$\sum_{j=1}^{2N} C_m^{s(j)} \lambda^{(j)} = \delta_{m0} (\delta^{s\sigma} \cos(\varphi) + \delta^{s\pi} \sin(\varphi)), \quad (8)$$

where $C_m^{s(j)} = D_m^{s(j)}$ for the Laue-case Bragg waves ($\gamma_m > 0$), and $C_m^{s(j)} = D_m^{s(j)} \exp(-i\omega\epsilon^{(j)}L)$ for the Bragg-case waves ($\gamma_m < 0$); L is the thickness of the plate, and φ is the deviation of the polarization plane of incident X-ray wave from \mathbf{e}^σ .

Substituting Eqs. (4) and (5) into (3) and evaluating the integral over the path of relativistic particle we found in Ref. [13] the following expression for the case of a thick crystal:

$$dN_{\mathbf{k},\omega}^s = \left(\frac{e\omega}{2\pi} \right)^2 \left| \sum_{s'=\sigma} \sum_{j=1}^{2N} (\mathbf{v} \cdot \mathbf{e}_h^{s'}) \lambda_s^{(j)}(\omega) \frac{D_h^{s'(j)}(\omega)}{Q^{(j)}(\omega)} \right|^2 \frac{d\omega}{\omega}. \quad (9)$$

Here

$$Q^{(j)}(\omega) = \omega(\gamma^{-2} + \Theta_1^2 + \Theta_2^2 + \Theta_v^2 + \Theta_s^2)/2 + \omega\gamma_h(\epsilon^{(j)} - \alpha_h), \quad (10)$$

parameter $\gamma = E/m$ is the γ -factor of relativistic particles, Θ_v is the angular deviation of particles from the exact incidence direction of multiple Bragg diffraction (it is introduced as a vector normal to \mathbf{v} because the deviations in two planes are possible), Θ_s is the mean square angle of multiple scattering of particle inside the crystal. The angles Θ_1 and Θ_2 determine the deviations of the emitted quanta from the exact incidence direction of multiple Bragg diffraction (see Fig. 1).

Eq. (9) contains two kinds of resonance functions. First, the diffraction amplitudes $D_h^{s(j)}$ have a maximum at the Bragg condition $\alpha_h = 0$. As known from the dynamical diffraction theory, this Bragg peak exhibits a halfwidth of the order of $d\omega/\omega \simeq |\chi_h|$ and, with increasing in $|\alpha_h|$, the amplitudes $D_h^{s(j)}$ decrease as $1/|\alpha_h|$. The second type of resonance function takes place at $\text{Re}(Q^{(j)}) = 0$ and corresponds to the synchronism between the phase velocity of generated X-rays and the velocity of relativistic particle. For N -wave PXR, there are $2(N-1)$ peaks of this kind corresponding to the resonances for different branches j of the dispersion equation. These Cherenkov peaks are sharper ($d\omega/\omega \simeq \text{Im}(\epsilon^{(j)}) \simeq \text{Im}|\chi_h| \simeq 10^{-2}|\chi_h|$) than the Bragg one,

but their peak intensity can be 10^2 – 10^3 that of the Bragg peak, especially in the case when the Cherenkov resonance takes place not far from the Bragg peak (when $|\alpha_h| \sim |\chi_h|$ providing $D_h^{s(j)} \simeq 1$). Then, the main contribution to the intensity of PXR is made by the set of very narrow peaks in Eq. (9), for which $\text{Re}(Q^{(j)}) = 0$ (see details in Ref. [13]). As follows from Eq. (10), the Cherenkov resonance can take place close to the Bragg peak at high energies of the particles, when $\gamma^{-2} \lesssim |\chi_h|$. This condition was just satisfied in experiments [17,19].

The angular distribution of PXR measured in the experiments [17,19] can be found by integrating Eq. (9) over the frequencies and polarizations of emitted X-ray quanta:

$$dN_k = \sum_{s=\sigma, \pi} \int_{-\infty}^{\infty} dN_{k,\omega}^s \frac{d\omega}{\omega}. \quad (11)$$

The integration in Eq. (11) must be carried out numerically within narrow bands in the vicinity of the Bragg peak and sharp Cherenkov peaks. For a more detailed information the reader is referred to Ref. [13].

4. Analysis of 4-wave experiment

As already established in Ref. [13], the implementation of multiple Bragg diffraction imposes very strong restrictions on the direction of incidence of X-ray quanta. Multi-wave Bragg diffraction of the order $N \geq 4$ splits into three independent two-wave Bragg diffractions if the X-rays are deviated from this direction to any side by the angle $(\Theta_1, \Theta_2) \geq |\chi_0| \sim 10^{-5}$ rad. As a result, the peculiarities of multi-wave PXR strongly depend on the direction of the relativistic beam incidence onto the crystal because the relativistic particles generate photons within a narrow cone relative to their velocity only. The multi-wave effects disappear while the electron beam is deflected through a wide angle $|\Theta_v^2| \gg \max(\gamma^{-2}, \Theta_s^2)$ from the direction of multiple Bragg diffraction. On the other hand, the multi-wave effects will not manifest themselves either if the incidence direction of relativistic particles explicitly coincides with that of the multi-wave diffraction because PXR quanta are not emitted explicitly along the particle movement.

Understanding of this basic requirement for the multiple Bragg diffraction was missing in Refs. [17,19] and the angle Θ_v was not measured. Moreover, taking into account the narrow angular range of multi-wave Bragg effects, we and some other researches had doubts about the responsibility of the multiple diffraction effects for the anomalies observed in Refs. [17,19]. Therefore, to estimate the maximum possible contribution from multi-wave effects to PXR angular spectra, we consider the situation where *the maximum exhibition* of these effects can be expected. That occurs when the electron beam is deflected from the exact multiple diffraction incidence by the angle $\Theta_v \approx (2.0, 0.5)$ mrad along Θ_1 and Θ_2 , respectively. In this case, the exact 4-wave Bragg condition is matched with one of two symmetrical maxima of two-wave PXR distribution (see Fig. 4). The 4-wave point in this figure is located at the intersection of two 3-wave lines (220)&(153) and (220)&(153). Our assumption can be quite realistic because the assumed angular deviation does not exceed the angle of multiple scattering of electrons in the crystal (cp. Table 1).

In Figs. 5a–c the cross sections of PXR angular distribution are presented as functions of Θ_1 for various values of Θ_2 , i.e. $\Theta_2 = (-1, 0, +1)$ mrad. The places of the sections are shown in Fig. 4 by dashed lines. According to Fig. 5, the multi-wave contributions can manifest themselves in very narrow angular regions only. The fine structure of these regions is given in Figs. 5d–f. One can see that the angular width of multi-wave peaks is by two or three orders of magnitude smaller than the total angular width of two-wave PXR distribution. Taking into account the fact that the angular averaging of the detector in the 4-wave experiment was much greater than the angular width of multi-wave peaks, it can be concluded that the multi-wave diffraction can not give any visible contributions to the experiment data.

The analysis of experimental geometry allows us to suggest that an asymmetry in the measured angular distribution could be due to a deflection of the experimental cross-section planes from the symmetry plane of the two-wave PXR angular distribution (see Fig. 4). It leads, for example, to the asymmetry between the peaks of two-wave angular distribution at various positions of a detector relative to the angle Θ_2 (cf. Figs. 5a and 5c).

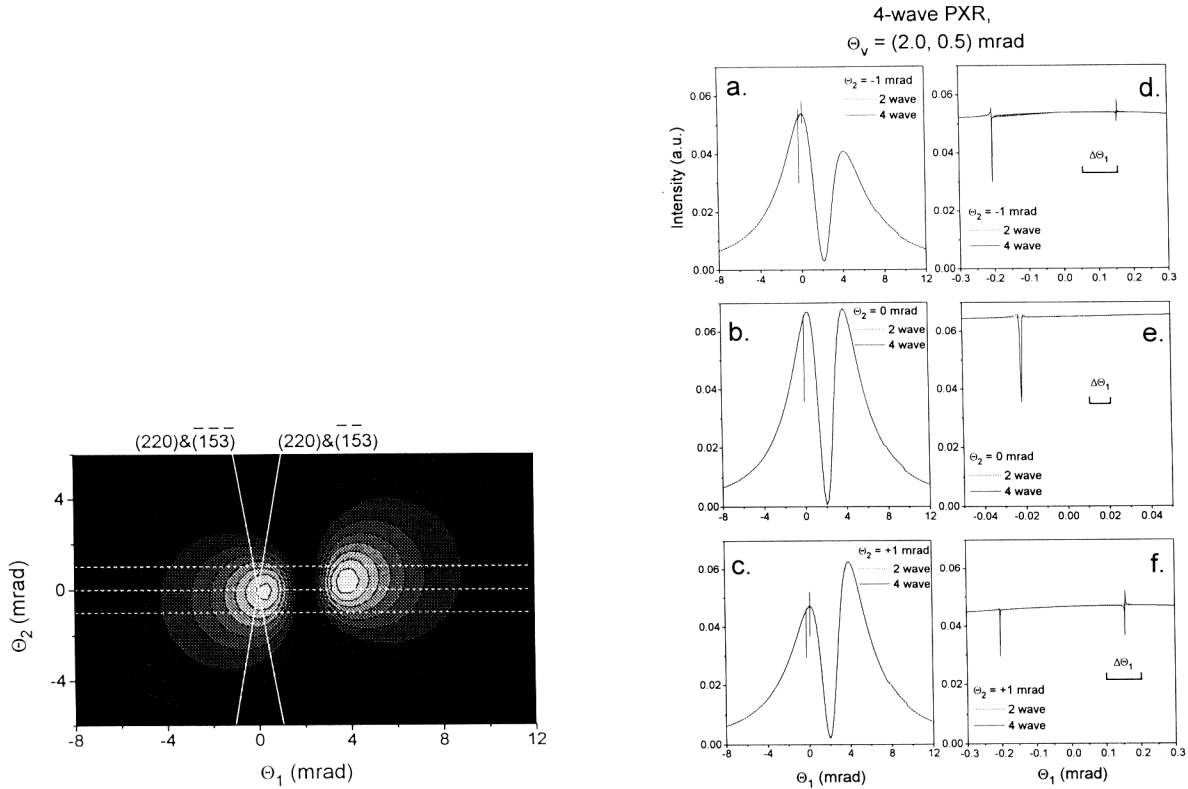


Fig. 4. (Left) The angular diagram of multi-wave diffraction conditions (white solid lines) in 4-wave case being matched with the equal-intensity contours of two-wave PXR. The dashed lines indicate the places of cross-sections shown in the next figure.

Fig. 5. (Right) Cross-sections of 4-wave PXR angular distribution for several values of Θ_2 : (a) -1 mrad, (b) 0 mrad, (c) $+1$ mrad. Plots (d)–(f) show the fine structure of multiwave peaks at (a)–(c) respectively. The interval marked $\Delta\Theta_1$ demonstrates the angular resolution of detector in experiment [17].

5. Analysis of 8-wave experiment

First of all, we have to note that the experimental geometry in Ref. [19] actually involved 12 waves. One can check that the incident X-ray wave satisfying the Bragg condition for (000) , (400) , (022) , $(02\bar{2})$, (202) , $(20\bar{2})$, (040) and (440) simultaneously matches the Bragg condition for (422) , $(42\bar{2})$, (242) and $(24\bar{2})$. Unfortunately, the 12-wave computations require unacceptably long time with our computer. Therefore, we simulate the experimental data in 8-wave diffraction approximation taking into account that the reflections of (422) family are relatively weak compared to (400) and (220) . To avoid a confusion, the experiment [19] is also referred to as the 8-wave one.

Another simplification used is neglecting the specular reflection effects for (202) and $(20\bar{2})$ diffracted waves which graze along (100) crystal surface. To increase the grazing angles, the small miscut of crystal surface by 1° along $[001]$ is allowed. In principle, the method of computing PXR spectra with grazing beams has been developed for 2-beam case in Refs. [6,32,33] and it can be extended for multi-beam case by combining [13] and the solution to the multiple Bragg diffraction problem with grazing beams obtained in Ref. [34]. However, the allowance of miscut provides considerable reduction of computations while the computed pattern cannot be qualitatively affected.

While analyzing the 8-wave effects in the PXR angular distribution we assume, as well as in the previous case, that the electron beam is deflected from the direction of the exact 8-wave diffraction condition through a small angle $\Theta_i = (4, -6)$ mrad, so that the 8-wave diffraction direction coincides with one of the two maxima of two-wave PXR distribution (see Fig. 6). Again, as in the previous section, the assumed deflection is reasonable because it does not exceed the mean square angle of the multiple scattering of electrons inside the

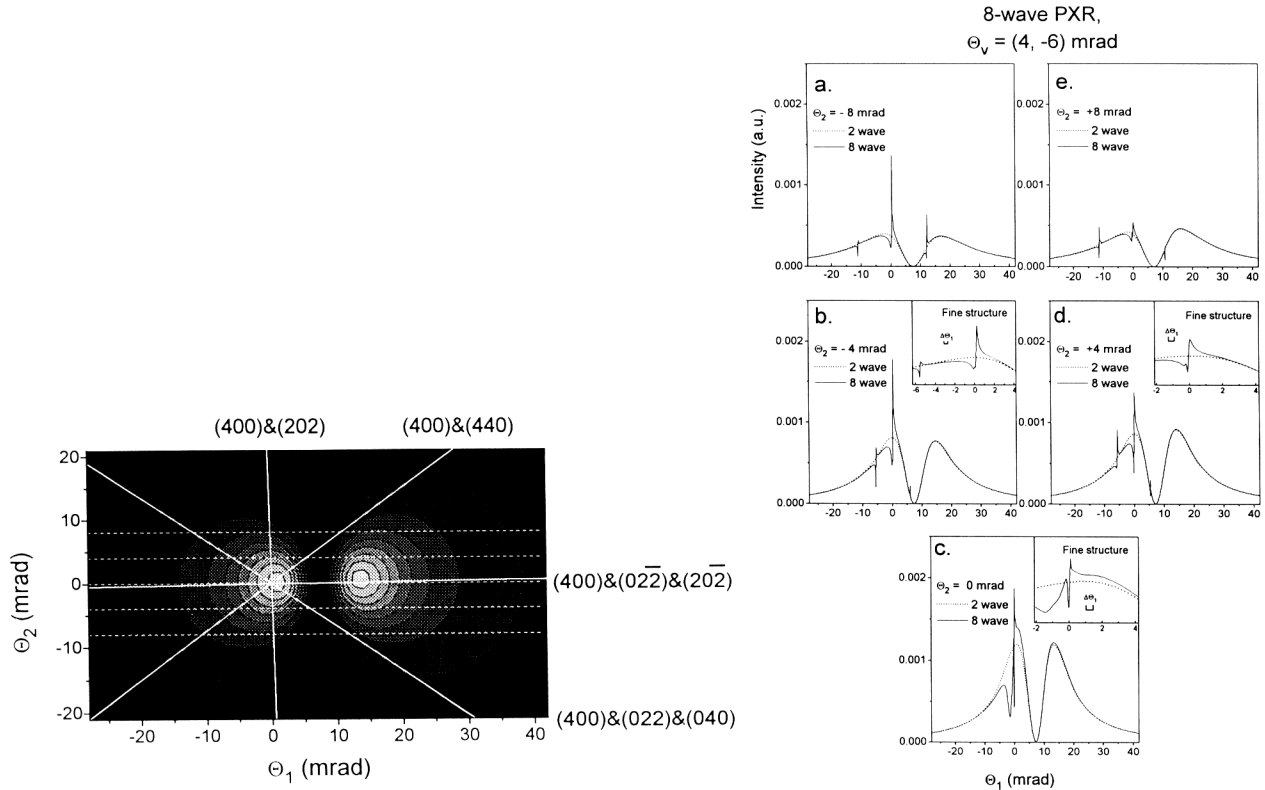


Fig. 6. (Left) The same as in Fig. 4 for 8-wave case.

Fig. 7. (Right) The same as in Fig. 5 for 8-wave case. The interval marked $\Delta\theta_1$ demonstrates the angular resolution of detector in experiment [19]. The insets show the fine structure of multi-wave peaks.

crystal (cp. Table 1). The straight lines in Fig. 6 labeled $(400)\&(202)$, $(400)\&(440)$, $(440)\&(02\bar{2})\&(20\bar{2})$ and $(400)\&(022)\&(040)$ correspond to the exact Bragg conditions for 3- and 4-wave Bragg diffraction. The point of their intersection ($\theta_1 = \theta_2 = 0$) corresponds to the exact 8-wave diffraction condition.

Thus, the deflection from the 8-wave diffraction direction leads to the decomposition of 8-wave PXR into several 3- and 4-wave PXR lines analogous to Kossel lines in a multiple Bragg diffraction pattern [29].

Far from the lines of multiple diffraction, the PXR angular distribution is formed by two-wave (400) diffraction only. On the other hand, the manifestation of multi-wave effects can be expected in the vicinity of the Kossel lines pointed out in Fig. 6. The 8-wave diffraction can contribute to PXR intensity in the near vicinity of point $\theta_1 = \theta_2 = 0$ only. This is a very important condition which should be taken into account while interpreting the experimental data.

Fig. 7 shows a series of cross-sections of PXR angular distributions along the dashed lines in Fig. 6. It is well seen that the contribution of multi-waves to PXR angular spectrum is much more prominent in comparison to the 4-wave situation considered above. In particular, the multi-wave peaks are about 10 times wider than in the 4-wave experiment. In addition, the multi-wave peaks now have rather long tails whose angular width is comparable with the total angular width of the two-wave PXR distribution. As a result, the integral contribution of multi-wave diffraction in the 8-wave case becomes much greater than in the 4-wave case.

The increase in the multi-wave peaks halfwidth in the 8-wave case is due to a lower frequency of generated X-rays. It is well known from the dynamical diffraction theory that the halfwidth of Bragg peaks is proportional to crystal dielectric susceptibility, the latter one possessing inverted square-law dependency on X-ray frequency: $\chi_h(\omega) \sim \omega^{-2}$. Therefore, while ω in the 8-wave case is approximately three times smaller than in the 4-wave one (see Table 1) the parameters χ_h and the halfwidth are increased by about an order. Furthermore, the

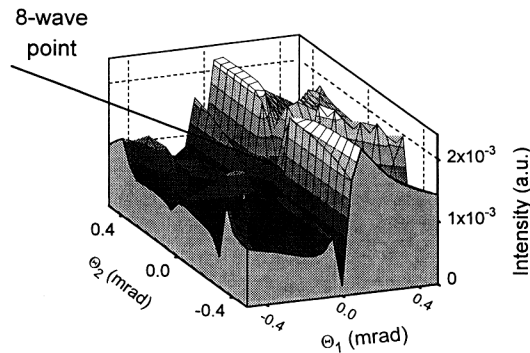


Fig. 8. Three-dimensional view of PXR intensity distribution in the vicinity of 8-wave diffraction condition.

appearance of long tails is supposed to be connected with the fact that the (440) reflection corresponds to the Bragg angle $\Theta_B = 90^\circ$ and the reflections (202) and $(20\bar{2})$ are formed by asymmetric diffraction. According to the dynamical diffraction theory the Bragg peaks in these cases are characterized by the great angular width.

As one can easily deduce from Fig. 7, the 8-wave diffraction alone does not essentially contribute to the total PXR angular distribution (see Fig. 7c). The observed enhancement of radiation intensity in the centre of the two-wave PXR distribution is formed, in general, by 3-wave diffraction on the planes (400)&(202) corresponding to a strip along the vertical line (400)&(202) in Fig. 6. This strip provides major anomalies in PXR spectra near $\Theta_1 = 0$ in all sections in Fig. 7. The traces of the other 3-wave and 4-wave lines are much less prominent. As a result, after averaging over the angular resolution of the detector and the angular spread of the electron beam, these peaks and pits will be rather smoothed out.

It is interesting to note that the multi-wave diffraction regions have, in their turn, fine structures. The fine structure of the multi-wave region near the angle $\Theta_1 = 0$ at various values of the angle $\Theta_2 = (-4, 0, +4)$ mrad, is presented in small insets in Figs. 7b–d, respectively. The reader can see on the inset in Fig. 7c that the 8-wave diffraction point itself is characterized by a narrow pit in the centre of the curve. It could be a reason for the experimentally observed splitting in the PXR distribution.

Thus, the PXR angular distribution under conditions of 8-wave diffraction can be characterized by very complex structure which is shown in Figs. 8 as a three-dimensional view.

As we have mentioned above, the angular space of the multi-wave effects is essentially smaller than that of the two-wave PXR angular distribution. It leads to a strong dependency of multi-wave effects on the position of the exact multi-wave diffraction point with respect to the maxima of the two-wave PXR and, consequently, on the direction of the relativistic beam incidence. The deflection of the relativistic particle from the exact multi-wave diffraction incidence by the angle $\Delta\Theta_i$, causes the shift of two-wave PXR angular distribution as a whole by the same angle relative to the multiwave point $\Theta_1 = \Theta_2 = 0$ (see e.g., Figs. 4 and 6). As a result of such deflection, the multiwave effects can make major contributions to one maximum of the two-wave PXR only. The second maximum will be formed generally by two-wave diffraction and will very slightly differ from the ordinary two-wave PXR distribution. This leads to an asymmetry in radiation density for two maxima of the two-wave PXR just in accordance with the experimental data (see Fig. 3a). Obviously, such asymmetry will not be observed if the centre of the electron beam incidence coincides with the exact direction of 8-wave diffraction.

Therefore, we assume that the symmetry centre of the electron beam in Ref. [19] was slightly deflected from $\langle 110 \rangle$ the crystallographic axis, i.e. from the exact 8-wave diffraction condition. Taking this assumption into account, the accordance between the calculated and the experimental results can be considered as satisfactory. Unfortunately, as mentioned above, the authors did not control this parameter during the experiments under consideration.

6. Conclusions

Thus, the comparison of computations where the multi-wave Bragg diffraction effects are taken into account and the experimental angular distributions observed in Refs. [17,19] allows us to draw the following conclusions:

- (i) The asymmetry in the PXR angular distribution observed in the experiment [17] cannot be explained by the influence of 4-wave diffraction. In this case, the widths of the multi-wave peaks are so small that their contributions to the formation of the PXR angular distribution can be neglected. The asymmetry of the two peaks in the observed two-wave distribution could be attributed to the deflection of the symmetry plane of two-wave angular distribution from the planes of experimental measurements.
- (ii) There is no doubt that anomalies in the angular distribution observed in the second experiment [19] could be caused by multiple Bragg diffraction effects. The comparison between experimental and calculated results shows their good qualitative agreement.

Unfortunately, we were not able to carry out the rigorous quantitative comparison because, on the one hand, the direction of the electron beam was not exactly fixed during the experiment and, on the other hand, we did not take into account all twelve Bragg reflections and did not average our results over the angular spread of the electrons on the grounds that this would have taken too much time for these calculations.

It should be noted, however, that the computations show the complex structure of multi-wave PXR regions which can be studied with a detector providing a better angular resolution.

The results obtained also confirm the possibility of increasing the PXR spectral-angular density within the narrow angular interval using multiple diffraction. The contributions from the multi-wave effects increase with decreasing Bragg frequencies due to the corresponding broadening of multi-wave diffraction peaks in the PXR angular distribution.

Acknowledgements

The authors are indebted to Professor V.G. Baryshevsky for stimulating discussions and for the permission to present his experimental data (Figs. 2 and 3). We are also pleased to thank Mrs. Viki Gibson for valuable remarks concerning the style of this article.

Appendix A. Reduction of Green function to solutions of the homogeneous problem

As well known, the spectral density of radiation per unit solid angle, denoted by $W_{n,\omega}$ (here $n = k/|k|$, and k and ω are the wave vector and the frequency of emitted quanta), may be obtained, if one knows the wavefield $E(\mathbf{r}, \omega)$ produced by a charge at a large distance from a crystal [35] (we assume $\hbar = c = 1$):

$$W_{n,\omega} = (r/2\pi)^2 |E(\mathbf{r}, \omega)|^2. \quad (\text{A.1})$$

With the help of Eq. (A.1) the differential number of quanta registered by a detector is calculated as $dN_{n,\omega} = W_{n,\omega} (d\omega/\omega) d\Omega$.

In order to determine the field $E(\mathbf{r}, \omega)$, one has to solve the Maxwell's equations:

$$-\nabla \times \nabla \times E(\mathbf{r}, \omega) + \omega^2 \hat{\varepsilon}(\mathbf{r}, \omega) E(\mathbf{r}, \omega) = -4\pi i \omega \mathbf{j}(\mathbf{r}, \omega), \quad (\text{A.2})$$

where $\hat{\varepsilon}(\mathbf{r}, \omega)$ is the tensor of dielectric susceptibility of the medium, and $\mathbf{j}(\mathbf{r}', \omega)$ is the Fourier transform of current produced by moving charge.

The transverse solution of Eq. (A.2) can be found by means of a Green function satisfying the equation of the form [36]:

$$\hat{G} = \hat{G}_0 + \hat{G}_0 (\omega^2/4\pi) (\hat{\varepsilon} - 1) \hat{G}. \quad (\text{A.3})$$

Here \widehat{G}_0 is the transverse Green function of Maxwell's equations with $\varepsilon = 1$; its explicit form is given, for example, in Ref. [37]:

$$\widehat{G}_0(\mathbf{r}, \mathbf{r}', \omega) = \frac{\exp(i k |\mathbf{r} - \mathbf{r}'|)}{|\mathbf{r} - \mathbf{r}'|} \widehat{I}, \quad (\text{A.4})$$

where \widehat{I} is the unit tensor, and $k = \omega/c$.

With the help of \widehat{G} , we can readily find the field of interest:

$$E_i(\mathbf{r}, \omega) = i \omega \int G_{il}(\mathbf{r}, \mathbf{r}', \omega) j_l(\mathbf{r}', \omega) d^3 r', \quad (\text{A.5})$$

where $i, l = x, y, z$.

We are interested in the field at a large distance from the target. Tending r to the infinity and taking into account Eq. (A.3) and the asymptotic form of \widehat{G}_0 :

$$\lim_{r \rightarrow \infty} \widehat{G}_0(\mathbf{r}, \mathbf{r}', \omega) = \frac{\exp(i k r)}{r} \exp(-i \mathbf{k} \mathbf{r}') \widehat{I}, \quad (\text{A.6})$$

we can write:

$$\widehat{G}(\mathbf{r}, \mathbf{r}', \omega) = \frac{\exp(i k r)}{r} \widehat{I} \left\{ \exp(-i \mathbf{k} \mathbf{r}') + \int \exp(-i \mathbf{k} \mathbf{r}'') \frac{\omega^2}{4\pi} [\widehat{\varepsilon}(\mathbf{r}', \mathbf{r}'') - 1] \widehat{G}(\mathbf{r}', \mathbf{r}'', \omega) d^3 r'' \right\}, \quad (\text{A.7})$$

or

$$\widehat{G}(\mathbf{r}, \mathbf{r}', \omega) = \frac{\exp(i k r)}{r} \widehat{I} \left\{ \exp(i \mathbf{k} \mathbf{r}') + \frac{\omega^2}{4\pi} \int \exp(i \mathbf{k} \mathbf{r}'') [\widehat{\varepsilon}^*(\mathbf{r}', \mathbf{r}'') - 1] \widehat{G}^*(\mathbf{r}', \mathbf{r}'', \omega) d^3 r'' \right\}^* \quad (\text{A.8})$$

Let us consider the expression in brackets of Eq. (A.8):

$$\Psi(\mathbf{r}', \omega) = \exp(i \mathbf{k} \mathbf{r}') + \frac{\omega^2}{4\pi} \int \exp(i \mathbf{k} \mathbf{r}'') [\widehat{\varepsilon}^*(\mathbf{r}', \mathbf{r}'') - 1] \widehat{G}^*(\mathbf{r}', \mathbf{r}'', \omega) d^3 r''. \quad (\text{A.9})$$

Representing the Green's function in the integrand, in its turn, as a series like (A.3) we can obtain

$$\begin{aligned} \Psi(\mathbf{r}', \omega) &= \exp(i \mathbf{k} \mathbf{r}') + \frac{\omega^2}{4\pi} \int \exp(i \mathbf{k} \mathbf{r}'') [\widehat{\varepsilon}^*(\mathbf{r}', \mathbf{r}'') - 1] \widehat{G}_0^*(\mathbf{r}', \mathbf{r}'', \omega) d^3 r'' \\ &+ \frac{\omega^4}{16\pi^2} \int \int \exp(i \mathbf{k} \mathbf{r}'') [\widehat{\varepsilon}^*(\mathbf{r}', \mathbf{r}'') - 1] \widehat{G}_0^*(\mathbf{r}'', \mathbf{r}''', \omega) \\ &\times [\widehat{\varepsilon}^*(\mathbf{r}'', \mathbf{r}''') - 1] \widehat{G}_0^*(\mathbf{r}', \mathbf{r}''', \omega) d^3 r'' d^3 r''' + \dots \end{aligned} \quad (\text{A.10})$$

Substituting \widehat{G}_0 in the form of (A.6) into (A.10) it is easy to show that the last term in (A.10) can be rewritten as:

$$\begin{aligned} &\frac{\omega^2}{4\pi} \int [\widehat{\varepsilon}^*(\mathbf{r}', \mathbf{r}'') - 1] \widehat{G}_0^*(\mathbf{r}', \mathbf{r}'', \omega) \\ &\times \frac{\omega^2}{4\pi} \left\{ \int \exp(i \mathbf{k} \mathbf{r}''') [\widehat{\varepsilon}^*(\mathbf{r}'', \mathbf{r}''') - 1] \widehat{G}_0^*(\mathbf{r}'', \mathbf{r}''', \omega) d^3 r''' \right\} d^3 r'' + \dots \end{aligned} \quad (\text{A.11})$$

As a consequence, the expression (A.10) transforms as:

$$\Psi(\mathbf{r}', \omega) = \exp(i \mathbf{k} \mathbf{r}') + \frac{\omega^2}{4\pi} \int [\widehat{\varepsilon}^*(\mathbf{r}', \mathbf{r}'') - 1] \widehat{G}_0^*(\mathbf{r}', \mathbf{r}'', \omega) \Psi(\mathbf{r}'', \omega) d^3 r''. \quad (\text{A.12})$$

Taking into account [see Eq. (A.6)] that $\widehat{G}_0^*(\mathbf{r}, \mathbf{r}', \omega) = \widehat{G}_0^{(-)}(\mathbf{r}, \mathbf{r}', \omega)$, where $\widehat{G}_0^{(-)}$ is the time-inverted Green function of Maxwell's equations with $\varepsilon = 1$, it turns out evidently the function $\Psi(\mathbf{r}', \omega)$ be a solution $e^s E^{(-)}(\mathbf{r}, \omega)$ of homogeneous Maxwell's equations, which can be written in a differential form as:

$$-\nabla \times \nabla \times \mathbf{E}^{(-)}(\mathbf{r}, \omega) + \omega^2 \varepsilon^*(\mathbf{r}, \omega) \mathbf{E}^{(-)}(\mathbf{r}, \omega) = 0. \quad (\text{A.13})$$

Here e_s are the unit polarization vectors ($s = \sigma, \pi$ and $e^\sigma \perp e^\pi \perp \mathbf{k}$) and the index $(-)$ denotes that the solution $\mathbf{E}^{(-)}(\mathbf{r}, \omega)$ contains at infinity the incoming spherical wave. If a wave is incident on a crystal with a finite thickness, then, with $r \rightarrow \infty$, the solution of (A.13) can be presented as:

$$\lim_{r \rightarrow \infty} \mathbf{E}_k^{(-)s}(\mathbf{r}, \omega) = e^s \exp(i \mathbf{k} \mathbf{r}) + \text{const} \frac{\exp(-i \mathbf{k} \mathbf{r})}{r}, \quad (\text{A.14})$$

As a result, at a large distance from the target the full Green function has an asymptote of the type:

$$\lim_{r \rightarrow \infty} [G_{il}(\mathbf{r}, \mathbf{r}', \omega)] = \frac{\exp(i \mathbf{k} \mathbf{r})}{r} \sum_{s=\sigma, \pi} e_i^s E_{kl}^{(-)s*}(\mathbf{r}', \omega), \quad (\text{A.15})$$

As well known from the reciprocity theorem (see e.g. Ref. [35]), the solution $\mathbf{E}_k^{(-)s}$ is related to the solution $\mathbf{E}_k^{(+s)}$ of homogeneous Maxwell's equations, describing a plane-wave scattering by a target (crystal), in the following way: $\mathbf{E}_k^{(-)s*} = \mathbf{E}_{-k}^{(+s)}$. Finally, with the help of (A.5) we arrive at:

$$E_i(\mathbf{r}, \omega) = \frac{\exp(i \mathbf{k} \mathbf{r})}{r} i \omega \sum_{s=\sigma, \pi} e_i^s \int \mathbf{E}_{-k}^{(+s)}(\mathbf{r}', \omega) \cdot \mathbf{j}(\mathbf{r}', \omega) d^3 r'. \quad (\text{A.16})$$

Substituting (A.16) into (A.1), we obtain the spectral energy of photons with polarization e^s as:

$$W_{n, \omega}^s = \left(\frac{\omega}{2\pi} \right)^2 \left| \int \mathbf{E}_{-k}^{(+s)}(\mathbf{r}, \omega) \cdot \mathbf{j}(\mathbf{r}', \omega) d^3 r \right|^2. \quad (\text{A.17})$$

The current $\mathbf{j}(\mathbf{r}', \omega)$ is expressed by definition as:

$$\mathbf{j}(\mathbf{r}, \omega) = \int e^{i \omega t} \mathbf{j}(\mathbf{r}, t) dt = e \int e^{i \omega t} \mathbf{v}(t) \delta(\mathbf{r} - \mathbf{r}(t)) dt. \quad (\text{A.18})$$

where e and $\mathbf{v}(t)$ are the charge and the velocity of the particle. Substituting (A.18) into (A.17) one arrives at Eq. (3) given in Section 3.

References

- [1] V.G. Baryshevsky and I.D. Feranchuk, Zh. Eksp. Teor. Fiz. 61 (1971) 944.
- [2] V.G. Baryshevsky and I.D. Feranchuk, Zh. Eksp. Teor. Fiz. 64 (1973) 760.
- [3] V.G. Baryshevsky and I.D. Feranchuk, Phys. Lett. A 57 (1976) 183.
- [4] V.G. Baryshevsky and I.D. Feranchuk, J. Phys. (Paris) 44 (1983) 913.
- [5] A.V. Ivashin and I.D. Feranchuk, Sov. Phys. - Crystallography (USA) 34 (1989) 39.
- [6] V.G. Baryshevsky, A.O. Grubich, I.D. Feranchuk and A.V. Ivashin, Nucl. Instr. and Meth. A 249 (1986) 306.
- [7] A. Caticha, Phys. Rev. B 45 (1992) 9541.
- [8] G.M. Garibyan and Y. Shi, Zh. Exp. Teor. Fiz. 61 (1971) 930 (1971).
- [9] G.M. Garibyan and C. Yang, Zh. Exp. Teor. Fiz. 63 (1972) 1198.
- [10] G.M. Garibyan and C. Yang, Nucl. Instr. and Meth. A 248 (1986) 29.
- [11] V.G. Baryshevsky and I.D. Feranchuk, Phys. Lett. A 102 (1984) 311.
- [12] I.Y. Dubovskaya, T.B. Ha and L.T. Hai, Phys. Status Solidi (b) 165 (1991) 571.
- [13] I.Y. Dubovskaya, S.A. Stepanov, A.Y. Silenko and A.P. Ulyanenkoff, J. Phys. C: Condens. Matter 5 (1993) 7771.
- [14] Y.N. Adishchev et al., Sov. Phys. - JETP Lett. (USA) 41 (1985) 361.
- [15] R.B. Fiorito et al., Phys. Rev. Lett. 71 (1993) 704.
- [16] R.B. Fiorito et al., Nucl. Instr. and Meth. B 79 (1993) 758.
- [17] V.P. Afanasenko et al., Phys. Lett. A 141 (1989) 311.
- [18] V.P. Afanasenko et al., Sov. Tech. Phys. Lett. 15 (1989) 13.

- [19] V.P. Afanasenko et al., *Sov. Phys. - JETP Lett. (USA)* 51 (1990) 242.
- [20] M.L. Ter-Mikaelian, *High Energy Electromagnetic Processes in Condensed Media* (Wiley-Interscience, New York, 1972).
- [21] A.V. Schagin, V.I. Pristupa and N.A. Khiznyak, *Phys. Lett. A* 148 (1990) 485.
- [22] H. Nitta, *Phys. Lett. A* 158 (1991) 270.
- [23] S. Asano et al., *Phys. Rev. Lett.* 74 (1993) 3247.
- [24] J. Freudenberger et al., *Phys. Rev. Lett.* 74 (1995) 2487.
- [25] X.K. Maruyama et al., in: *Proc. 1993 Part. Accel. Conf.*, Washington, DC, 1993, Vol. 2, p. 1620.
- [26] M.A. Piestrup et al., *J. Appl. Phys.* 73 (1993) 5152.
- [27] S.L. Chang, *Multiple Diffraction of X-rays in Crystals* (Springer, Berlin, 1984).
- [28] V.G. Kohn, *Phys. Status Solidi (a)* 54 (1979) 375.
- [29] Z.G. Pinsker, *Dynamical Scattering of X-Rays in Crystals* (Springer, Berlin, 1981).
- [30] I.D. Feranchuk and A.V. Ivashin, *J. Phys. (Paris)* 46 (1985) 1981.
- [31] V.G. Baryshevsky and I.Y. Dubovskaya, *J. Phys. C: Condens. Matter* 3 (1991) 2421.
- [32] A.A. Andriyanchik, I.Y. Dubovskaya and A.N. Kaminsky, *J. Phys. C: Condens. Matter* 3 (1991) 5579.
- [33] A.A. Andriyanchik, V.G. Baryshevsky and A.N. Kaminsky, *Nucl. Instr. and Meth. B* 83 (1993) 482.
- [34] S.A. Stepanov and A.P. Ulyanenko, *Acta Cryst. A* 50 (1994) 579.
- [35] L. Landau and E. Lifshitz, *Electrodynamics of Continuous Media* (Pergamon, London, 1960).
- [36] J.R. Taylor, *Scattering Theory. The Quantum Theory on Nonrelativistic Collisions* (Wiley, New York, 1970).
- [37] P.M. Morse and H. Feshbach, *Methods of Theoretical Physics* (McGraw-Hill, New York, 1953).